Inherently Matched Arrays Over Wide Scan Ranges, Part I: Self-Dual Radiating Element

Roee Geva and Raphael Kastner

Abstract — Self-dual media (SDM) have been shown to exhibit reflection-free characteristics, and, as such, they enable the design of inherently matched devices. In this article, we show a design of an array-radiating element whose active reflection coefficient is annulled over a wide scan range and whose bandwidth depends only on the characteristics of the materials involved.

1. Introduction

Nonreflective properties of balanced materials that have identical electric and magnetic parameters [1–3] are well known. Recently, we also showed that slab-like media with distinct electric and magnetic self-dual symmetries (SDMs) [4] also produce zero backscatter. SDMs are characterized by the property $\varepsilon_r\ (x,\ y) = \mu_r(-y,\ x)$ at any cross-sectional plane $z = \text{const}$ within the slab, $\hat{z}$ being the normal to the slab surface. This condition defines a class of planar interfaces that remain unchanged if 1) the structure is tilted 90° about the z-axis and 2) any electric material with permittivity ε_r is replaced by a magnetic material with the permeability $\mu_r = \varepsilon_r$ and vice versa.

In this article, we use the nonreflective property for the design of inherently matched phased arrays over large scan range. It is shown that self-duality is helpful in producing a slowly varying element pattern that translates into very low active reflection coefficient values over wide scan and frequency ranges. A radiating element with conceptual near–perfect electrical conductor (PEC) and near–perfect magnetic conductor (PMC) walls is introduced in Section 2. In this element, most of the energy is funneled through a central narrow bore. Simulations show that if such an element could be produced and excited, its pattern would indeed be close to ideal for wide scan arrays. A more close-to-realistic element is presented in Section 4. Here, we employ magnetic metasurfaces such that the entire structure is fabricated of actual materials. The element would be fed with a square transverse electromagnetic (TEM) waveguide that is again a self-dual structure, also comprising realistic materials, as shown in Section 3. With this element and feeder, the door appears to be open for the design of full-phased array systems, including feeding power dividing networks [10]. Finally, conclusions are drawn in Section 5.

Manuscript received 3 December 2022.

Roee Geva and Raphael Kastner are with the School of Electrical Engineering, Tel Aviv University, 69978 Tel Aviv, Israel; e-mail: kast@tauex.tau.ac.il.

2. Conceptual Array-Radiating Element

The radiating element presented in Figure 1 is conceptual in the sense that it is simulated with theoretical magnetic (as well as electric) materials of unlimited bandwidth. It is in fact an open-ended quasi-TEM waveguide with the top and bottom (blue) regions being dielectric and the complementary green regions being magnetic. When this element is subject to a $\pm z$-directed plane wave incidence, the power within the slab appears to be funneled primarily through the center bore. The size of the bore is one-tenth of the side of the element, making it deeply sub-wavelength in our 3-GHz to 10-GHz range. A pure y-directed linearly polarized TEM wave would have been achieved within the bore if perfect conductors had been used. Otherwise, the E and H fields in the bore are approximately related by the free space impedance relationship, forming a dynamic quasi-TEM (marginally slow) wave; see Figure 2. To highlight the leakage into the material surrounding the bore, we choose in this figure $\varepsilon_r = \mu_r = 6$ rather than the parameters in Figure 1. As for the aperture fields, a buildup of near-field modes is necessary to satisfy the boundary conditions at the transition. These aperture distributions are seen in Figure 3 for the parameters in Figure 2.

This element is embedded in a tightly packed two-dimensional infinite array. It is fed by Floquet-type waveguides whose walls are coincident with the external surfaces of the elements and that adhere to the scan direction. In the case of broadside radiation, such a feed is identical to a square TEM waveguide comprising top and bottom PECs and sideways PMCs. The wide scan range is verified through the very slowly

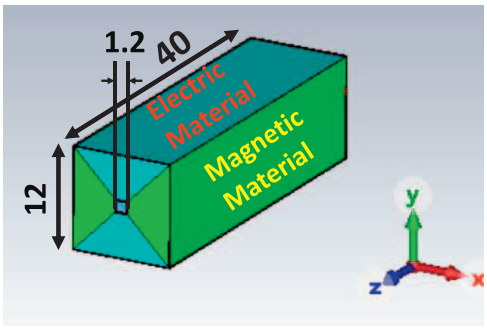

Figure 1. Conceptual SDM element. The top and bottom (blue) prism-like regions are near-PECs with $\varepsilon_r' = 1,\ \sigma_e = 10^7$ s/m, and the side (green) regions are near-PMC with $\mu_r' = 1,\ \sigma_h = 1.42 \cdot 10^{12}\ \Omega/$m such that $\varepsilon_r'' = \mu_r'' >> 1$. Azimuth and elevation cuts for the element patterns are the x-z and y-z planes. Dimensions are in millimeters.

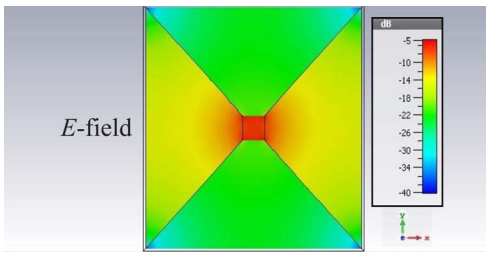

Figure 2. *E*-field profile at a cross section located 5.5 mm from the aperture into the SDM element similar to Figure 1, except $\varepsilon_r = \mu_r = 6$ at $f = 7.5$ GHz. A close-to-uniform distribution is seen over the bore, indicating the quasi-TEM mode achieved with the near-perfect conductors.

varying embedded element pattern that also traces the locus of the scanned main beam peak of the array (see explanations in [5, section 10.1] and [6, chapter 1, section 2.1]). This pattern is simulated in two different fashions. In the first one, we trace the peaks of the total array pattern over all scan angles (θ_0) for a given ϕ_0. These data are extracted from the infinite array calculation and are shown in Figure 4a for $\phi_0 = 0$ (*H*-plane) and Figure 4b for $\phi_0 = 90°$ (*E*-plane) over the above-mentioned frequency range. The second calculation is based on the excitation of a single element in the array, while all others are terminated. To this end, we simulate two semi-infinite arrays shown in Figure 5. For the pattern in the *H*-plane, we model the array in Figure 5a. Here, the array comprises 15 elements in the *x*-direction and is infinite in the *y*-direction. Feeding the center column of this array with uniform phase makes it possible to obtain embedded element patterns that

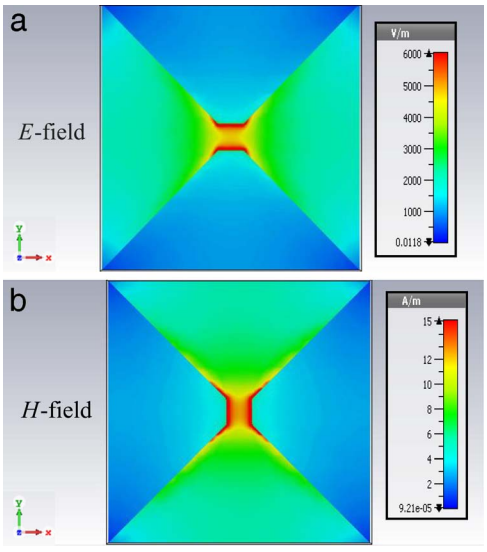

Figure 3. Aperture field distributions at $f = 7.5$ GHz over the input surface of the element similar to Figure 1 except $\varepsilon_r = \mu_r = 6$, subject to normal plane wave incidence: (a) Electric field (*E*-field) over the aperture, showing the appearance of higher-order modes needed to enable the reflectionless transition from the guiding structure with the profile shown in Figure 1 to free space. (b) Magnetic aperture field (*H*-field).

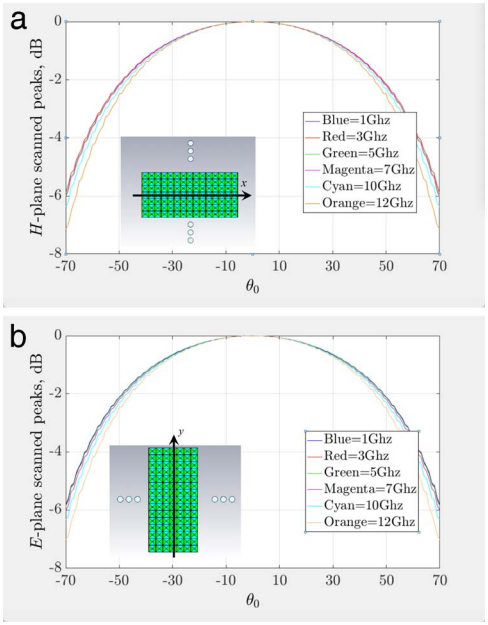

Figure 4. Element patterns for the element in Figure 1 embedded in an infinite array, obtained as the locus of the peaks of scanned beams over the 1 GHz to 12 GHz range. (a) *H*-plane (azimuth). (b) *E*-plane (elevation).

virtually overlap the ones shown in Figure 4 and are omitted here for brevity. Incidentally, the beamwidth at both *E*- and *H*-planes are the same, which can be beneficial for certain applications.

3. Options for Magnetic Metasurfaces and TEM Waveguides

Media that have duals require the incorporation of magnetic materials, in particular, ones that provide near-PMC boundary conditions. Since no magnetic monopoles have been found to date in nature, magnetic metasurfaces are now in use (e.g., [7, 8]). We select several derivatives of mushroom-type unit cell [8] configuration with additions of dielectric and (conceptual) magnetic filler materials and lumped capacitors for the purpose of size reduction. Those structures should exhibit near-PMC response within a certain bandwidth, defined, for example, by the standard criterion of reflection phases within $\pm 90°$. Among the several metasurfaces tested, four are shown in Figure 6.

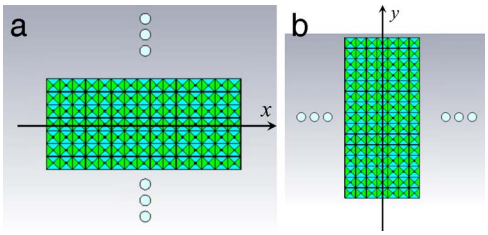

Figure 5. (a) $15 \times \infty$ and (b) $\infty \times 15$ arrays used to generate the phase and amplitude distributions.

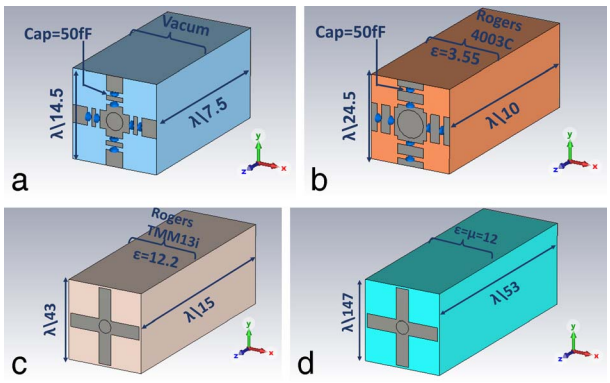

Figure 6. Initial development of magnetic metasurfaces with progressively decreasing unit cell size. Size of the unit cell is reduced progressively from options UC1 through UC4. Magnetic surface is defined at the front plane with the printed cross. (a) Option UC1: vacuum-filled unit cell with connecting capacitors. (b) UC2: dielectric-filled (RO4003C laminate) unit cell with capacitors. (c) UC3: dielectric-filled (TMM13i laminate) unit cell without capacitors. (d) UC4: smallest dimension achieved with $\varepsilon_r' = \mu_r' = 12$ laminate.

Examining their corresponding phase response with respect to angle of incidence (Figure 7), we note that the angular dependence tends to become moderate as the size of the unit cell is reduced (becoming closer in nature to lumped element).

A TEM waveguide with PEC top and bottom surfaces and magnetic metasurfaces as sidewalls, essentially based on [9], is shown in Figure 8a. To combat edge effects, we use smaller unit cells in the metasurface selected above and also add dummy

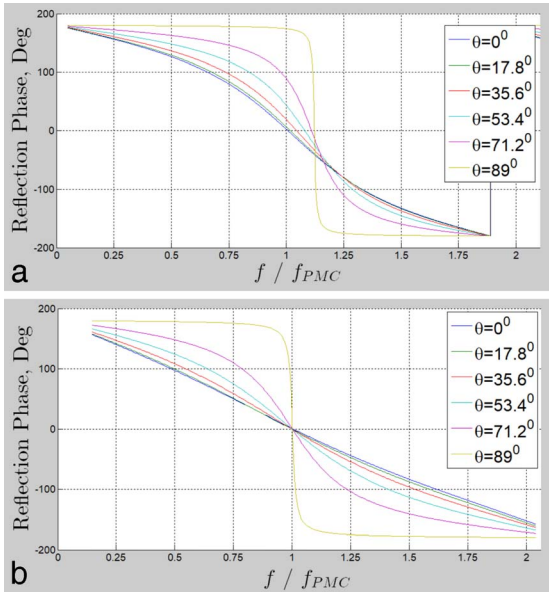

Figure 7. Phase of reflected waves in the structures of Figures 6a and 6b, showing gradual improvement, expressed in a flattening process of the reflection phase angular response over the transition from Figure 6a toward Figure 6d. f_{PMC} is the resonant frequency where the field is reflected in-phase for a normally incident plane wave. (a) UC1. (b) UC4.

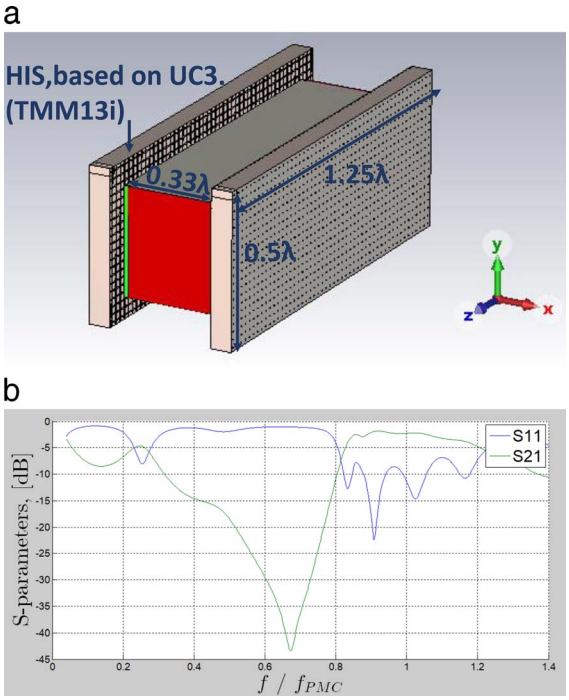

Figure 8. TEM waveguide 3D model with its small-unit cell side walls and the addition of dummy elements. Inside and outside dimensions are 0.3 λ and 0.5 λ, respectively, including the dummy elements. (a) 3D structure of TEM waveguide. (b) *S*-parameters.

elements that protrude above and below the waveguide to better emulate an infinite surface. Performance of the metasurface as a near-PMC wall is characterized by the level of suppression of the tangential magnetic field over the surface. We also verify the important performance criterion of uniformity of the transverse fields across the waveguide cross section. *S*-parameter results (Figure 8b). show an extra dielectric loss of approximately 1.5 dB.

4. An Option for a Radiating Element

Consider now a nonreflective self-dual metasurface based on the cross section of the waveguide in Figure 1. This element comprises a back-to-back arrangement of finite trapeze-looking slices of the magnetic UC4 metasurface of Figure 6d shown in green plus the complementary PEC parts; see Figure 9a. We also add a slim absorber (sapphire) buffer between the electric and magnetic portions that helps improve the actual symmetry. Embedded at any cross section of a TEM waveguide of the type described in Section 3 (Figure 9b), it is perfectly transparent for the fundamental mode. Specifically, when placed at the open end of the waveguide, it can serve an inherently matched array element. All incident energy on this surface is funneled through a central bore, as seen in Figure 9c. Figure 9d shows scattering parameter results for three different cases of bore dimensions, namely, $d_{\text{in}} = \lambda/12$, $\lambda/10$, and $\lambda/8$. The outer dimension of the unit cell is maintained as $d_{\text{in}} = \lambda/3$ for all cases. As one can note,

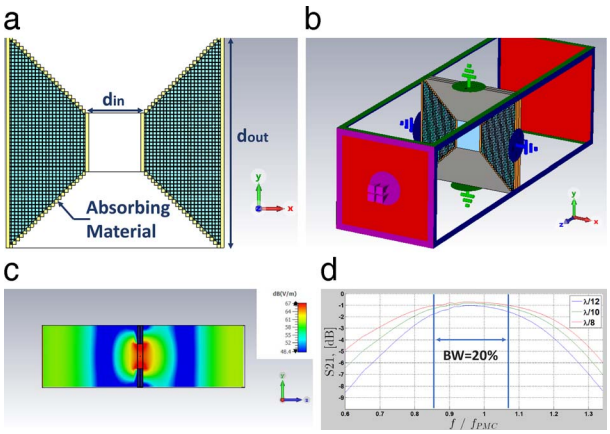

Figure 9. Simulation setup and results of the thin prism-like transparent surface embedded in a TEM waveguide. (a) Nonreflecting surface with two back-to-back magnetic UC4 metasurfaces (Figure 6d), shown in green, with gray PEC areas, plus the slim absorber in yellow. (b) Embedding of the surface of Figure 9a in a TEM waveguide. (c) Side view of the *E*-field in Figure 9b. Field density within the bore is ∼8 dB higher than in the TEM guide due to funneling. (d) *S*-parameters of the prism-like element. The *S*-parameters results help predict the finite structure frequency range.

transmission bandwidth across the element improves as the bore is wider due to the effect of higher modes generation at the surface for smaller bores.

5. Conclusions

The slowly varying element patterns in Figure 4 indicate the feasibility of scanning arrays with wide scan range. Most notably, effects of scan blindness would be inherently eliminated. We also note that in transmit mode, high power density in the very narrow bore may result in a limitation to the total power-handling capability. This effect would be evaluated on a case-by-case basis, depending on the input power as it is divided among the elements and on the ratio of power density in the bore versus power of a single element. In Figure 9c, this ratio is about 8 dB, which is not too prohibitive. This element would be integrated with a beamforming network designed within the same TEM environment; see initial steps in an accompanying paper [10].

6. References

1. W. W. Salisbury, "Absorbent Body for Electromagnetic Waves," US Patent 2599944 (A), June 10, 1952.
2. V. H. Weston, "Theory of Absorbers in Scattering," *IEEE Transactions on Antennas and Propagation*, **11**, 5, September 1963, pp. 578-594.
3. R. Kastner, "Dispersivity of Balanced Near Zero Permittivity and Permeability (EMNZ) Medium," *IEEE Transactions on Microwave Theory and Techniques*, **64**, 10, October 2016, pp. 3108-3112.
4. N. Mohammadi Estakhri, N. Engheta, and R. Kastner, "Electromagnetic Funnel: Reflectionless Transmission and Guiding of Wave Through Subwavelength Apertures," *Physical Review Letters*, **124**, January 2020, p. 033901.
5. P-S. Kildal, *Foundations of Antenna Engineering*, Gothenburg, Sweden, Kildal Antenna AB, 2015.
6. N. Amitay, V. Galindo, and C-P. Wu, *Theory and Analysis of Phased Array Antennas*, New York, Wiley, 1972.
7. S. B. Glybovski, S. Tretyakov, P. A. Belov, Y. S. Kivshar and C. R. Simovski, "Metasurfaces: From Microwaves to Visible," *Physics Reports*, **634**, May 2016, pp. 1-72.
8. A. Li, S. Singh and D. Sievenpiper, "Metasurfaces and Their Applications," *Nanophotonics* **7**, 6, February 2018, pp. 989-1011.
9. F-R. Yang, K-P. M and Y. S. Qian, "A Novel TEM Waveguide Using Uniplanar Compact Photonic-Bandgap (UC-PBG) Structure," *IEEE Transactions on Microwave Theory and Techniques*, **47**, 11, November 1999, pp. 2092-2098.
10. R. Geva and R. Kastner, "Inherently Matched Arrays Over Wide Scan Range, Part II: Self-Dual Power Splitters," companion paper in this volume.